Lewis acid sites incorporation promotes CO_2 electroreduction to multicarbon oxygenates over B-CuO nanotubes

Han Zhu [a,*], Jingwen Hu [a], Zhili Zhang [a], Zechao Zhuang [b], Jiace Hao [a], Fang Duan [a], Shuanglong Lu [a], Xiaofan Wang [a], Mingliang Du [a]

[a] Key Laboratory of Synthetic and Biological Colloids, Ministry of Education, School of Chemical and Material Engineering, Jiangnan University, Wuxi 214122, PR China
[b] Department of Chemical Engineering, Columbia University, New York, NY, 10027, USA

ARTICLE INFO

ABSTRACT

Herein, we designed a C_{2+}-producing catalyst by incorporating Lewis acid boron dopant into porous copper oxides nanotubes (B-CuO NTs) via a convenient electrospinning−calcination method. The B-CuO NTs catalyst achieved a 60.5% C_{2+} Faraday efficiency (FE) including 47% of ethanol, a 4-fold increase over CuO in a flow cell at − 0.6 V vs reversible hydrogen electrode (RHE). In situ characterizations demonstrate that the strong ability for *CO adsorption on B-CuO NTs facilitates the hydrogenation to the *CHO intermediate and promotes the C-C coupling further to *OCCHO intermediate via the proton-coupled electron transfer reactions. Theoretically calculations demonstrate that B doping induced polarized charge redistribution could suppress the *CHO transfer to C_1 products by reducing the energy barrier for further OC-CHO coupling. This work provides a comprehensive understanding of Lewis acid B doping effect on regulating the C-C coupling pathway and improving the C_2 selectivity.

1. Introduction

Developing sustainable and renewable energy conversion technology to solve the urgent energy crisis and environment problems has recently been reported as one of the most important challenges [1,2]. Clean electricity powered CO_2 electroreduction (CO_2RR) into value-added chemical feedstocks is an attractive near-zero-emission approach to promote an artificial carbon cycle [3]. Accompanying by complicated reaction mechanisms towards different products, CO_2RR require highly efficient catalysts to activate inert CO_2 molecules and to produce specific products with high selectivity [4,5]. Various heterogeneous catalysts including metal/metal alloys [6–8], metal-free catalysts [9], molecular catalysts [10,11], and their derivative [12,13] have been developed for CO_2RR. Many products ranging from C_1 (CO, formate, methanol and methane) [14–16] to C_{2+} (ethylene, ethanol, acetate and acetone) [17,18] can be achieved via CO_2RR. Xu and Wang group have designed polypyrrole-modified oxygen vacancy-rich Bi_2O_3 nanosheet and diethylenetriamine-functionalized mosaic Bi nanosheets to produce formate through CO_2 electroreduction [19,20]. However, converting CO_2 directly into high energy density and widely applicability multicarbon oxygenates and hydrogencarbon (C_{2+}) is of great

significance for fundamental research [19]. Unfortunately, the formation of the C-C coupling is a key challenge in CO_2RR, which require extremely condition to obtain C_{2+} than C_1 products [20].

At present, nanostructured Cu-based materials are the only known catalysts that can convert CO_2 to C_{2+} products in significant amounts [21]. It is because that Cu has the optimal binding energy toward crucial intermediates, which is neither "too strong" nor "too weak". The binding strength of *CO intermediate and its subsequent hydrogenation into the hydrogenated species on the catalyst surface determines whether the H_2, C_1 or C_{2+} are the final products [22]. Several important strategies including morphology regulation [23], structure engineering [24], alloying [25], faceting [26], and surface ligands modification [27] have been explored to manipulate selectivity on Cu-based catalysts. Recently, oxide-derived Cu (OD-Cu) catalysts present unprecedented C_{2+} selectivity and low overpotential due to their rough morphology, grain boundaries and large defect density, and undercoordinated active sites [28–30]. However, the reduction of bound proton intermediates (*H) into H_2 serves as a parasitic competing reaction alongside the CO_2RR process, and the OD-Cu strategies only focused on regulating the adsorption strengths of *CO intermediates but ignore the suppression for competitive HER, resulting in the insufficient selectivity for C_{2+}

* Corresponding author.
E-mail address: zhysw@jiangnan.edu.cn (H. Zhu).

products (<40%). Therefore, realizing high selectivity for C_{2+} products especially multicarbon oxygenates remain great challenge and the exploring advanced electrocatalysts and revealing the underlying mechanism is also of great concern.

Herein, we designed porous copper oxides nanotubes with incorporation of Lewis acid boron dopant (B-CuO) by a convenient electrospinning−calcination method as a promising model to increase C_{2+} and lower C_1 product selectivity for CO_2RR. The B-CuO NTs catalyst achieved a 60.5% C_{2+} FE including 47% of ethanol, a 4-fold increase over CuO in a flow cell at − 0.6 V vs reversible hydrogen electrode (RHE), which is superior higher than those of recently reported Cu-based catalysts. *In situ* Raman and ATR-FTIR spectra demonstrate that the strong ability for *CO adsorption facilitates the hydrogenation to the *CHO intermediate and promotes the C-C coupling further to *OCCHO intermediate on B-CuO NTs via the proton-coupled electron transfer reactions. The FE for H_2 on B-CuO NTs were simultaneously significantly decreased to 14.4% under − 0.6 V, a 2-fold decrease over CuO NFs (30.6%) due to the mutual repulsion between incorporated Lewis acid B sites and protons. DFT calculations demonstrate that strong polarized charge redistribution by B doping could suppress the *CHO transfer to C_1 products by reducing the energy barrier for OC-CHO coupling. This work provides a comprehensive understanding of Lewis acid B doping effect on regulating the C-C coupling pathway and improving the C_2 selectivity.

2. Experimental section

2.1. Chemicals

Copper nitrate trihydrate ($Cu(NO_3)_2 \cdot 3\ H_2O$, 99%), potassium hydroxide (KOH, 95%), polyvinylpyrrolidone (PVP, M_w = 1 300 000), dimethyl sulfoxide (C_2H_6SO, 99.7%) and deuterium oxide (D_2O, 99.9%) were purchased from Shanghai Macklin Biochemical Co., Ltd. Boric acid (H_3BO_3, 99.8%), N, N′-dimethylformamide (DMF, 99%), ethanol anhydrous (C_2H_6O, 99.7%) and acetone (C_3H_6O, 99.7%) were purchased from Sinopharm Chemical Reagent Co., Ltd. Argon (Ar, 99.999%) and carbon dioxide (CO_2, 99.9995%) were ordered from Xinxiyi Technology Co., Ltd. (Wuxi, China). Ultrapure water (Milli-Q) was used to prepare the aqueous solution. All the reagents were used without any further purification.

2.2. Synthesis of the H_3BO_3-$Cu(NO_3)_2$/PVP precursor nanofiber membrane

Electrospinning technology was used to prepare the precursors solutions. In a typical procedure, 3.6 mM $Cu(NO_3)_2 \cdot 3\ H_2O$ and 1.8 mM H_3BO_3 were added into 16 g mixture solution containing DMF and ethanol (the total mass of metal salt was 1 g, and the ratio of DMF and ethanol was 1:1). Then 2 g PVP powder was dissolved in the above solution after one hour and then vigorously stirred for 12 h at room temperature to get a homogeneous solution. After that, the mixed solution was transferred to 10 mL injection syringes with a needle diameter of 0.7 mm. During the electrospinning process, the temperature and humidity of the electrospinning machine (YFSP-T, Tianjin Yunfan Technology Co., Ltd.) were controlled at 30 °C and 40%. Besides, the anode voltage and cathode voltage were 20 kV and 2 kV, the distance between needle and metal roller was 18 cm and the injection rate was 0.5 mL h^{-1}. After 15 h, the as-obtained B-Cu precursor PVP nanofiber membrane was placed in the oven at 80 °C overnight to remove the residual moisture.

2.3. Synthesis of the B substituted-CuO NTs

The H_3BO_3-$Cu(NO_3)_2$/PVP precursor nanofiber membrane was heated to 200 °C with a heating rate of 2 °C min^{-1} and maintained for 3 h under air atmosphere using a home-built chemical vapor deposition

(CVD) system. Then, the membrane was continuously heated to 500 °C with 2 °C min^{-1} under air atmosphere. Subsequently, the membrane was naturally cooling to room temperature and the B doped CuO nanotubes (B-CuO NTs) were obtained. Besides, to synthesize a series of B-CuO NTs with different morphologies, the B-Cu precursor PVP nanofiber membrane was calcined at different temperatures (300 °C, 500 °C and 700 °C).

2.4. Synthesis of the CuO NFs

4.1 mM $Cu(NO_3)_2 \cdot 3\ H_2O$ and 2 g PVP powder were added into 16 g mixture solution of DMF and ethanol and then vigorously stirred at room temperature to get a homogeneous solution. After electrospinning process, the Cu precursor PVP nanofiber membrane was heated to 200 °C with a heating rate of 2 °C min^{-1} and maintained for 3 h under air atmosphere. Then, the membrane was continuously heated to 500 °C with 2 °C min^{-1} under air atmosphere. Subsequently, the membrane was naturally cooling to room temperature and the CuO nanofibers (CuO NFs) were obtained.

2.5. Materials characterizations

The morphologies of the as-prepared samples were collected by the field-emission scanning electron microscope (FE-SEM Hitachi S-4800, Japan) with an acceleration voltage of 3 kV and the transmission electron microscope (TEM, JEM-2100 plus, Japan) operated at 200 kV. The STEM images, mapping and energy dispersive X-ray spectrum (EDX) were acquired with a scanning transmission electron microscope (STEM, JEOL JEM-F200, Japan), using an acceleration voltage of 200 kV. The phase and structure of the samples were conducted on a Bruker AXS D8 X-ray diffraction (XRD) using Cu-K_α (λ = 0.154 nm) with the scan rate of 5° min^{-1}. X-ray photoelectron spectroscopy (XPS) measurements were analyzed by Thermo Scientific K-Alpha with a monochromatic Al K_α source (1486.6 eV). The content of the Cu and B in B-CuO/NTs was obtained by an inductively coupled plasma optical emission spectroscopy (ICP-OES, Ahilent 5110). Electron spin resonance (ESR) measurement was performed on a Bruker EMXplus spectrometer. Infrared spectra (IR) of the B-CuO/NTs was carried out using a Nicolet 6700 Fourier transform infrared (FTIR) spectrophotometer with the scan range from 800 to 1600 cm^{-1}. Raman measurements were conducted on the confocal Raman microscope with a 532 nm laser. Thermogravimetric analysis (TGA) was conducted on the instrument 1100SF (Mettler Toledo) with a ramp rate of 20 °C min^{-1} from room temperature to 500 °C under air atmosphere. The specific surface area of B-CuO and CuO was measured by the Brunauer−Emmett−Teller (BET) isothermal technique. The pore size distributions of the samples were calculated by the Barrett−Joyner−Halenda (BJH) method. Cu K-edge absorption spectra (EXAFS) of B-CuO NTs, CuO, Cu_2O and Cu foil were obtained using the BL08U1-A operated at 500 eV with the injection current of 100 mA at Shanghai Synchrotron Radiation Facility (SSRF). The in situ Raman measurements were carried out using a Renishaw inVia confocal microscope at the excitation laser wavelength of 785 nm. Prepared catalysts served as the working electrode, Ag/AgCl and Pt wire worked as the reference electrode and counter electrode. The flowing KOH solution (1 M) with continuous CO_2 injection acted as the electrolyte. The in situ Raman spectra were collected using chronoamperometry tests from − 0.2 to − 1 V (vs. RHE) and each potential maintained at least 10 min for sufficient reaction. The in situ ATR FT-IR test was performed using a Thermo Scientific Nicolet 6700 FT-IR spectrometer with the range at 1100–4000 cm^{-1}. The in situ FT-IR spectra were obtained using chronoamperometry tests from − 0.1 to − 0.9 V (vs. RHE) with kept at least 10 min for each potential.

2.6. Electrochemical measurements

The CO_2 reduction reaction (CRR) were performed using an Autolab

302 N electrochemical workstation with a standard three-electrode system conducted on a commercial flow cell (Gaossunion) in 1 M KOH solution at room temperature. To prepare the ink of working electrode, 3 mg catalyst and 15 μL Nafion (5 wt%) were dispersed in the 300 μL ethanol solution and ultrasonicated for 30 min to obtain a homogeneous dispersion of catalyst ink. Then, the ink was airbrushed onto a carbon paper (Sigracet 29 BC) as working electrode (2 ×0.5 cm) and the loading mass is 0.5 mg cm^{-2}. The Ag/AgCl (3.0 M KCl) and RuO$_2$ (airbrushed onto a carbon paper, loading mass: 0.5 mg cm^{-2}) worked as the reference electrode and counter electrode, respectively. An anion exchange membrane (PAA-3-PK-130) was used to separate the anolyte and catholyte. The volumes of electrolyte in anode and cathode compartment were both 50 mL. In addition, the electrolyte (1 M KOH) was circulated through the flow cell by a bump with flowing rate of 10 mL min^{-1} during the CRR process. Besides, the CO$_2$ gas was controlled at 20 mL min^{-1} using the flowmeter. To analyze the gas-phase products of working electrode, the cathodic compartment was directly connected to the gas chromatograph (GC, Agilent 7890B) equipped with TCD and FID detectors. The liquid products were quantitatively analyzed by ^{1}H NMR on a Bruker 400 MHz (AVANCE III) spectrometer with D$_2$O and DMSO acted as solvent and internal standard. The Faradaic efficiency (FE) of products were calculated by the equation: FE=eF×n/Q, where e is the number of transfer electrons, F is the Faraday constant (96485 C mol^{-1}), n is the moles of the products, and Q is the total charge in the CRR process. The linear sweep voltammetry (LSV) was performed with sweep rate of 5 mV s^{-1}. The electrochemical impedance spectroscopy (EIS) was conducted at the open circuit voltage in the range from 10^{-2} Hz to 10^5 Hz. To obtain the electrochemical active surface area (ECSA), cyclic voltammetry (CV) technique was carried out with different scan rate to calculate the electrochemical double layer capacitances (C$_{dl}$). All potentials were converted to the RHE according to Nernst equation: E$_{(vs.\ RHE)}$ = E$_{(vs.\ Ag/AgCl)}$ + E$_{Ag/AgCl}$ + 0.0591 x pH.

2.7. Theoretical Calculations

The free energies and electronic structure calculations were all performed by density functional theory (DFT) with the generalized gradient approximation (GGA) and Perdew-Burke-Ernzerhof (PBE) exchange-correlation functional in the Vienna ab initio simulation program (VASP) code. The kinetic energy cutoff was set to 400 eV [31–33]. The convergence criterion for geometry optimization and electronic structure was set to be 0.03 eV/Å and 10^{-5} eV, respectively. A 2 × 2 × 1 K-point was used for the free energy calculation. The CuO (111) surface was modeled with a p (2 ×2) supercell slab. The three-layer slab model was used with the 1 lower layers fixed and the 2 upper layers relaxed to mimic a semi-infinite solid. A vacuum layer of 15 Å along the z-direction was used to avoid the interaction between the neighboring layers. We use the computational hydrogen electrode (CHE) model proposed by Nørskov [34] to calculate the Gibbs free energy of the intermediates [34], for each intermediates, the Gibbs free energy ΔG can be calculated using:

$$\Delta G = \Delta E + \Delta ZPE - T\Delta S + Ue + \Delta G_{pH}$$

where ΔE is the reaction energy difference between the reactants and the products, ΔZPE is the zero-point energy, ΔS is the entropy change, T represents the finite temperature, e is the charge transferred, U is the applied potential, and ΔG$_{pH}$ is considered as the correction free energy of H$^+$. The zero-point energy and the entropy change were calculated from vibrational frequencies.

3. Results and discussion

3.1. Materials synthesis and characterization

We first used density functional theory (DFT) calculations to investigate an in-depth understanding of the advantages for B-CuO on regulating the C-C coupling and promoting the C$_{2+}$ products compare to the CuO. Table S1 show the B loading of B-CuO NTs is 0.56 wt%, which was measured by inductively coupled plasma optical emission spectroscopy (ICP-OES). Based on the ICP-OES results, the stable configurations of CuO (111) and B-CuO (111) slabs were shown in Fig. 1a. Charge density differences (Fig. 1b) suggest that the B-CuO NTs exhibits abundant charge depletion on B site and charge accumulation around Cu sites, suggesting the strong polarized charge redistribution. The Bader charge analysis (Table S2) further demonstrate that with B doping, the average Bader charger on Cu sites in B-CuO NTs (0.90997) is lower than that of CuO NFs (0.92685), indicating the considerably electron transfer from B to Cu atoms. Density of states (DOS) (Fig. S1) indicate that the d band center of B-CuO exhibits slightly positive shift to Fermi level compared to that of CuO NFs, suggesting the low oxidation state of Cu^{2+} towards Cu$^+$ caused by the electron transfer between B and Cu sites.

The Gibbs free energy (ΔG) for the key intermediate of *CHO and *OCCHO towards C$_1$ and C$_{2+}$ products was calculated and presented in Fig. S2 and Fig. 1c. The correspondingly optimal structures of adsorbed intermediates on CuO NFs and B-CuO NTs were displayed in Fig. S3 and Fig. S4. The hydrogenation reaction of *CO reduction to *CHO is the key intermediate for generating C$_1$ products, the energy battier (ΔG) for *CO converting to *CHO on CuO NFs is 0.198 eV, which is lower than that on B-CuO NTs (0.395 eV), suggesting that the CO$_2$RR pathway on CuO NFs tend to form C$_1$ products. Meanwhile, the formation of *OCCHO intermediates on B-CuO NTs surface (−1.144 eV) is significantly easier than that on CuO NFs (0.203 eV), implying that the CO$_2$RR on the B-CuO surface prefers to form C$_2$ products. The adsorption energies of *CO, *CHO and *COCHO species on CuO NFs and B-CuO NTs catalysts were summarized in Table S3. The schematic illustration of CO$_2$RR pathways on CuO NFs and B-CuO NTs were shown in Fig. 1d. The results clearly demonstrate that the polarized charge redistribution through B doping can suppress the *CHO transfer to C$_1$ products by reducing the energy barrier for OC-CHO coupling.

Fig. S5 illustrates the synthesis procedure of B-CuO NTs via a convenient electrospinning-calcination method. Briefly, copper nitrate (Cu(NO$_3$)$_2$) and boric acid (H$_3$BO$_3$) served as the Cu and B sources were dissolved in the homogeneous polyvinylpyrrolidone (PVP) solution. After electrospinning process, the obtained membrane was calcinated at 500 °C under air atmosphere using a chemical vapor deposition (CVD) furnace system, and the final B-CuO NTs were formed after calcination for 3 h. X-ray diffraction (XRD) patterns of CuO NFs without B doping (Fig. 2a) exhibit the monoclinic CuO phase (PDF#48–1548). In comparison, the 2θ degree for (11−1) and (111) planes of CuO phase in B-CuO NTs display slightly shifts, indicating the incorporation of B atoms into CuO crystal lattice. Fig. 2b shows the corresponding atomic structure model of CuO and B-CuO crystals. Scanning electron microscopy (SEM) image of the H$_3$BO$_3$-Cu(NO$_3$)$_2$/PVP precursor nanofibers indicate an unique three-dimensional (3D) network structure consist of random distributed nanofiber with smooth surface (Fig. S6). After calcination at air atmosphere for 3 h, the as-synthesized B-CuO NTs display unique porous tubular structure formed by closely packed B-CuO nanocrystals (Fig. 2c-e). Meanwhile, the average diameter of B-CuO NTs was 160 ± 20 nm (Fig. S7), exhibiting significant shrinkage compared to the precursor nanofibers. SEM and TEM images (Fig. S8 and Fig. S9) of CuO NFs display nanofiber morphology without tubular structures.

The N$_2$ adsorption-desorption isotherm curves reveal that the B-CuO NTs exhibit a Brumaire-Emmett-Teller (BET) surface area of 94.9 m^2·g^{-1}, which is 3.72 times than that of CuO (25.5 m^2·g^{-1}) (Fig. S10). Besides, the pore size distribution of the B-CuO/NTs is approximately 8.75 nm, which is lower than that of CuO (11.51 nm), suggesting a typical mesopores porous structure of B-CuO NTs. The porous and hollow structures of B-CuO could facilitate the diffusion of CO$_2$ molecules, which could further improve the CRR activity. Thermogravimetric analysis (TGA) was used to investigate the calcination process from Cu(NO$_3$)$_2$-H$_3$BO$_3$/PVP NFs to B-CuO NTs. As shown in
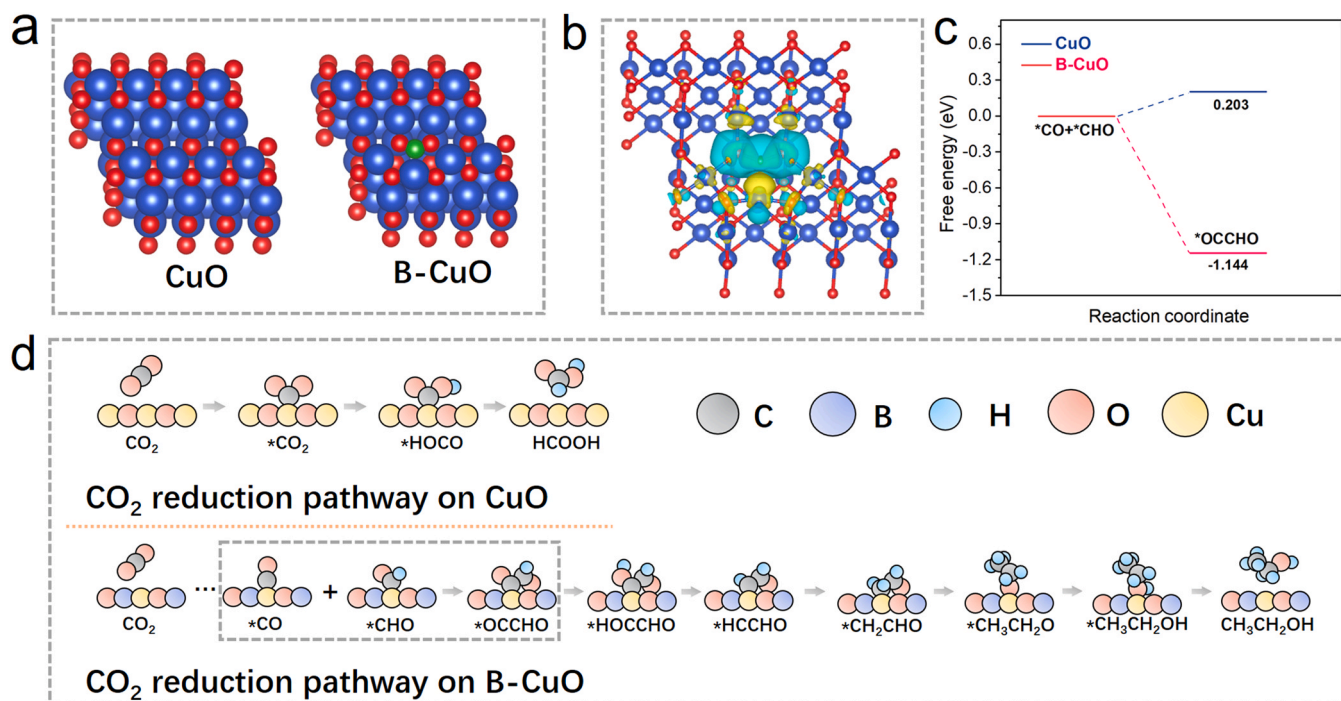
Fig. 1. (a) The stable configurations of CuO (111) and B-CuO (111) slabs. (b) The chager density difference between Cu (blue) and B (green) atoms. The cyan part represents the charge depletion and the yellow part represents the charge accumulation. (c) Gibbs free energy profiles of *CO coupling *CHO to form *OCCHO on CuO NFs and B-CuO NTs. (d) The schematic illustration of CO_2RR pathways on CuO and B-CuO.

Fig. S11, ~10% weight loss can be observed between 50 °C and 120 °C, which is ascribed to the evaporation of absorbed moisture, residual solvent and crystal water of metal nitrate. The subsequent weight loss at temperature from 120 to 235 °C was assigned to the decomposition of the metal salts, forming the copper oxides and boron oxides under air atmosphere. The prominent weight loss around 240 °C was ascribed to the decomposition of PVP nanofibers and the formation of B-CuO.

Fig. 2f shows the high-resolution transmission electron microscopy (HRTEM) image of B-CuO NTs, and the distinct interplanar spacings of 2.3 Å and 2.8 Å corresponds to the (111) and (110) planes of CuO. Fast Fourier transform (FFT) image exhibit the (111), (110) and (11−1) planes of monoclinic CuO phase. Selected area electron diffraction (SAED) image (Fig. 2g) of the B-CuO NTs shows the diffraction rings for (110), (11−1), (111), (20−2) and (202) planes, suggesting the polycrystallinity of B-CuO NTs with closed packed nanocrystals, which were in accordance with the XRD results. Scanning TEM energy disperse X-ray spectroscopy (STEM-EDX) element mapping images (Fig. 2h) reveal the well distribution of B, Cu and O elements through the whole B-CuO NTs. Line-scan EDX spectra of B-CuO NTs exhibits the relatively strong intensities for the element distribution of B, Cu and O at the edge of B-CuO NTs, suggesting the formation of unique tubular structures. As shown in Fig. S12 and Table S1, the B loading of 0.55 wt% for B-CuO NTs was measured by EDS spectra, which was in according with the ICP-OES results (0.56 wt%).

Chemical states of B-CuO NTs were further investigated by X-ray photoelectron spectroscopy (XPS) and X-ray-induced Auger electron spectroscopy (XAES). Fig. S13 shows the XPS survey spectra of B-CuO NTs. As shown in Fig. 3a, the Cu 2p XPS spectra of CuO NFs can be deconvoluted into six peaks. The peaks located at 933.4 and 953.3 eV are attributed to Cu $2p_{3/2}$ and Cu $2p_{1/2}$ of Cu^{1+}, while the peaks at 934.4 and 954.3 are ascribed to Cu $2p_{3/2}$ and Cu $2p_{1/2}$ of Cu^{2+} [35]. Besides, other peaks are matched with the satellite peaks. Notably, the Cu 2p XPS spectra of B-CuO NTs also exhibit the similar peaks for Cu^{1+} and Cu^{2+} with binding energies (BEs) at 932.6, 933.7, 952.1 and 953.7 eV, respectively, suggesting the co-existence of Cu^{2+} and Cu^+. The BEs for main peaks of Cu^{1+}/Cu^{2+} exhibit positively shifts when compare to that

of CuO NFs, indicating the electron transfer occurred in B-CuO NTs, which was according with the changes in Cu LMM Auger spectra of CuO and B-CuO (Fig. S14) [36]. In addition, B-CuO NTs shows decreased intensity in the surface composition of Cu^{2+} from 37.6% to 33.4% and increased intensity of Cu^{1+} from 5.9% to 10.8% compared to CuO NFs (Table S4), revealing the significant electron transfer from B to Cu due to the B doping. B 1 s XPS (Fig. 3b) reveals the B-O bonds in B-CuO NTs with BE at 191.6 eV, suggesting the successfully doping of B in CuO nanocrystals [37]. Meanwhile, Fourier-transform infrared (FT-IR) spectroscopy (Fig. S15) of B-CuO NTs also confirm the existence of B-O bonds around 1300 cm^{-1} [38]. O 1 s XPS spectra (Fig. 3c) can be deconvoluted into three peaks centered at 529.8, 531.4 and 533.8 eV, corresponding to the lattice O^{2-}, oxygen vacancies (O_{2-2} or O^-) and surface-adsorbed O_2, respectively [39]. According to the content of peak areas (Table S5), the proportion for oxygen vacancies in B-CuO NTs were calculated to be 62.77%, which is higher than that of CuO NFs (46.11%), demonstrating that the B dopant can induce the formation of oxygen vacancies in B-CuO NTs. The oxygen vacancies were further investigated by electron spin resonance (ESR) spectroscopy (Fig. S16), and the B-CuO NTs uniquely shows a symmetrical ESR signal at g = 2.002, suggesting the electron trapping at oxygen vacancies. The results indicate that the B incorporation with CuO lead to the enhanced electron transfers between B and Cu lead to the formation of low oxidation states of CuO with oxygen vacancies.

Cu K-edge X-ray absorption near edge structure (XANES) of B-CuO NTs (Fig. 3d) indicate that the absorption edge position of B-CuO NTs is closer to CuO reference. Meanwhile, the edge position of B-CuO NTs indeed exhibits a slightly shift towards that of Cu_2O reference caused by the B doping, suggesting that the Cu atoms in B-CuO NTs were mostly present in both + 1 and + 2 valence states. K space Extended X-ray absorption fine structure (EXAFS) spectra (Fig. S17 and Fig. S18) of B-CuO NTs is similar with CuO reference, suggesting that no metallic Cu were formed. As shown in Fig. 3e, the Cu K-edge Fourier transform of the X-ray absorption fine structure (FT-EXAFS) spectrum of B-CuO NTs shows two predominant peaks at 1.5 and 2.6 Å, corresponding to the Cu-O and Cu-Cu bonds. The peak intensity for Cu-O bond in B-CuO NTs is
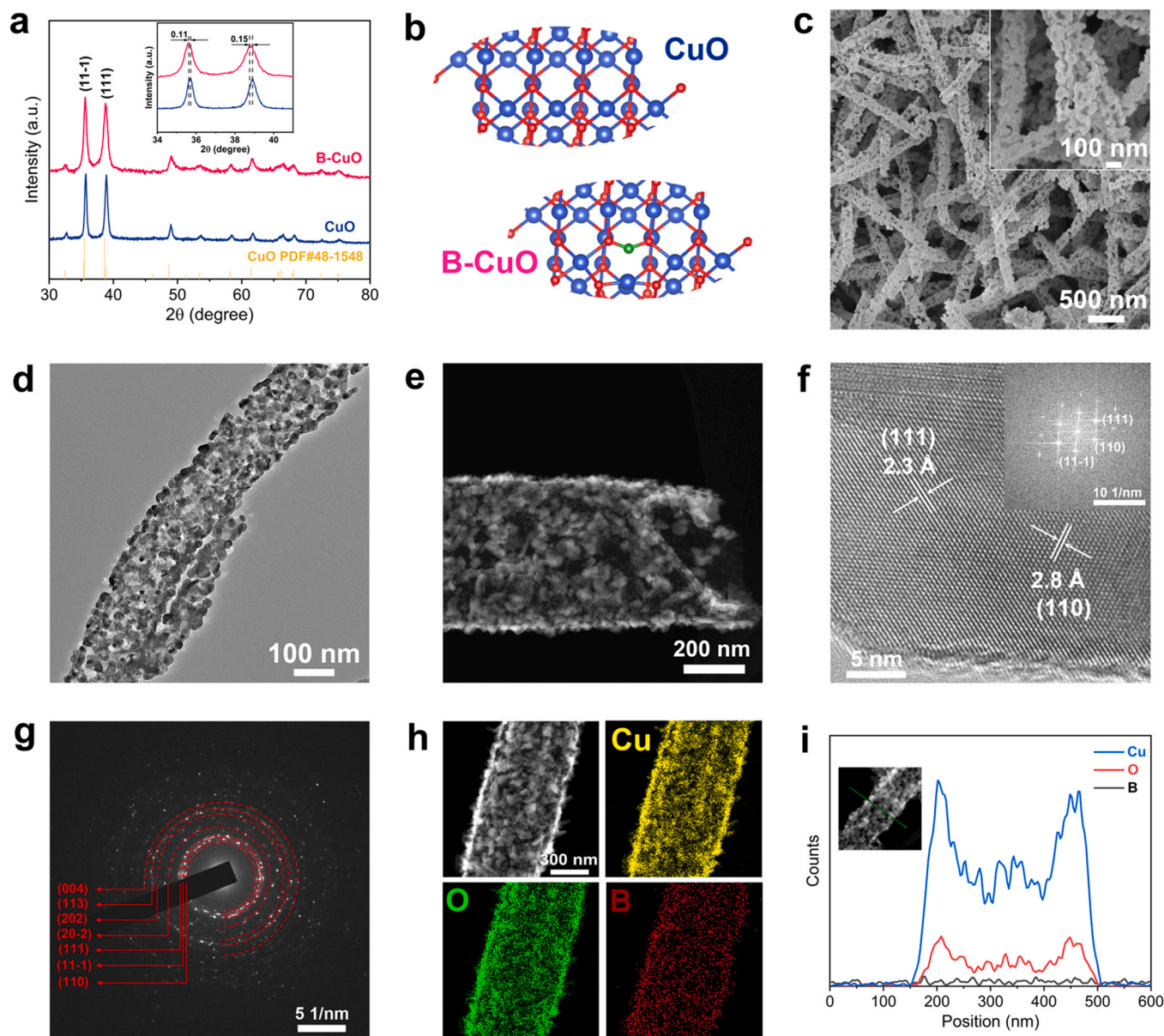
Fig. 2. (a) XRD patterns of CuO NFs and B-CuO NTs. (b) The atomic structure model of CuO NFs and B-CuO NTs. The blue, red and green balls represent Cu, O and B atoms, respectively. (c) FE-SEM, (d) TEM and (e) STEM images of the B-CuO NTs. (f) HRTEM and (g) SEAD images of B-CuO NTs. The inset in f is the corresponding FFT image of B-CuO NTs. (h) STEM-EDX element mapping images and (i) line-scan EDX spectra of the B-CuO NTs.

lower than that in CuO, indicating a lower degree of oxidation due to the electron transfer from B dopant, in agreement with the XPS results [40]. The Cu K-edge EXAFS fitting curves (Fig. 3f, Fig. S19 and Table S6) show that the coordination number (CN) of Cu-O in B-CuO NTs is 2.97, which is lower than that in CuO (4.0). In addition, the Cu-Cu in B-CuO NTs shows higher CN of 7.82 than that of CuO 6.0. The bond lengths of Cu-O and Cu-Cu in B-CuO NTs are 1.95 Å and 2.92 Å, respectively. The significant changes in CNs of Cu-O and Cu-Cu between B-CuO NTs and CuO further confirm the less oxidation state of Cu in B-CuO NTs. The Cu k-edge wavelet transform (WT)-EXAFS of B-CuO NTs (Figs. 3g-3j) exhibits one intensity maximum at 5.6 Å, corresponding to the Cu-O bond, which shows a negative shift in wave vector K compare to that of CuO (6.0 Å) due to the decreased CN of Cu-O caused by B doping. Moreover, the lower CNs of Cu-O and higher CNs of Cu-Cu leads to the strong intensity for Cu-Cu in B-CuO. The XAFS results manifest the low oxidation states of Cu in B-CuO caused by the significant electron transfer between the B and Cu, in well agreement with the XPS results.

3.2. Electrocatalytic CO_2 reduction performance

The CO_2RR performance of B-CuO NTs and CuO NFs were performed in a flow cell using 1 M KOH as electrolyte. All potentials were calibrated to the RHE. As shown in Fig. 4a, the linear sweep voltammetry (LSV) curves of B-CuO NTs exhibit higher current density and smaller onset potential under CO_2 atmosphere than that of N_2 atmosphere. Notably, the B-CuO NTs only require -0.98 V to reach the industrial current density of 200 mA cm^{-2}, which is three times higher than that of CuO NFs (73 mA cm^{-2}), suggesting the excellent CO_2RR activity. The selectivity of different products was further measured by online gas chromatography (GC, Fig. S20) and ^{1}H nuclear magnetic resonance (^{1}H NMR, Fig. S21). Fig. S22 presents the Faradaic efficiencies (FEs) of various products including H_2, CO, C_2H_4 and formate, methanol, acetate, ethanol, acetone in applied potentials from -0.3 V to -0.9 V. The detailed information about the FEs of various productions was displayed in Table S7 and Table S8. As shown in Fig. 4b, the FE for H_2 of B-CuO NTs was 14.4%, the FE for C_1 products (CO, methanol, formate) was
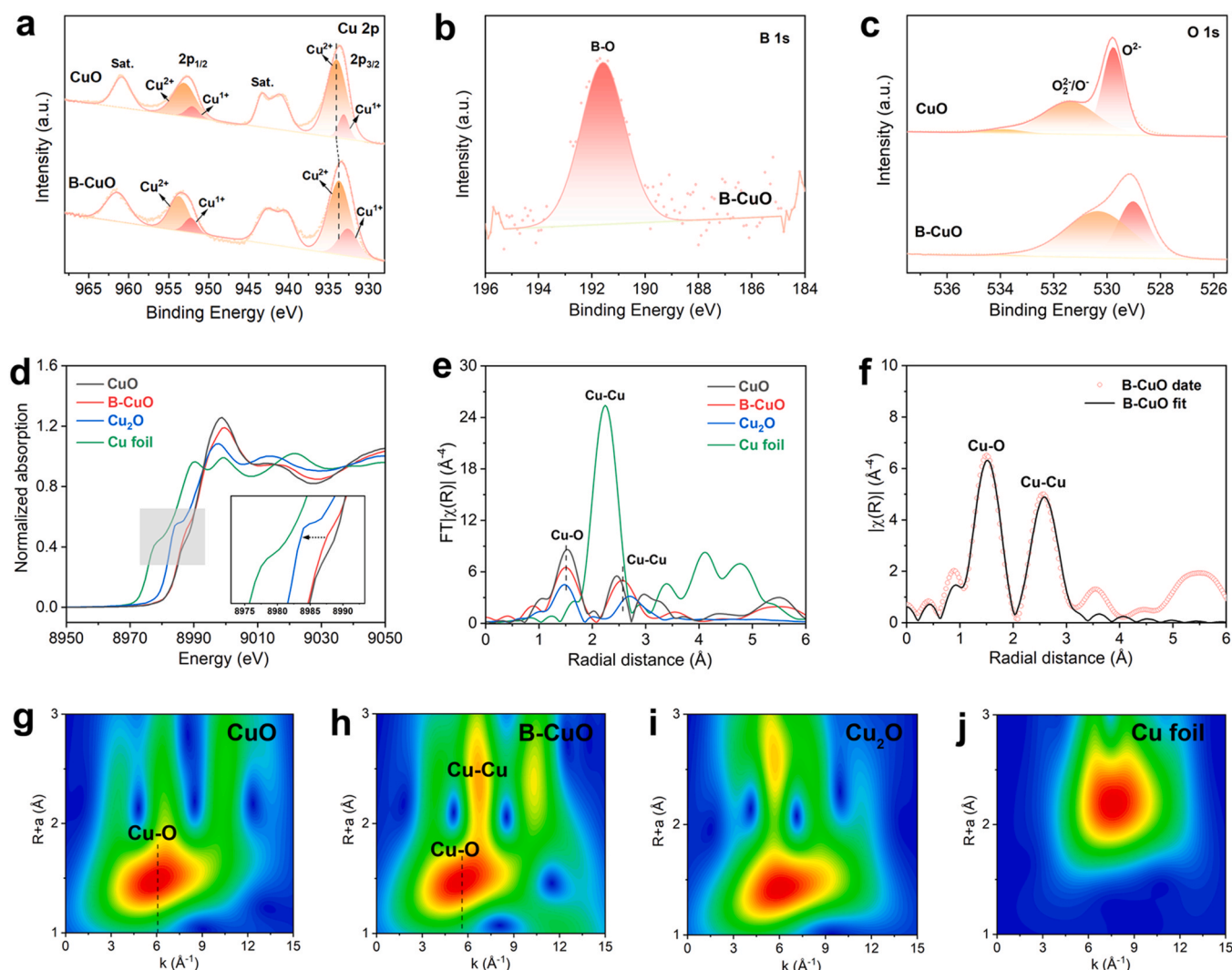
Fig. 3. (a) Cu 2p, (b) B 1 s, and (c) O 1 s XPS spectra of CuO NFs and B-CuO NTs. (d) Cu K-edge XANES spectra and (e) Cu K-edge Fourier transform EXAFS spectra of B-CuO NTs, CuO, Cu_2O and Cu foil. (f) The corresponding fitting curve of B-CuO NTs. (g-j) Cu k-edge WT-EXAFS spectra of B-CuO NTs, CuO, Cu_2O and Cu foil.

14.2%, the FE for C_2 products (ethanol and acetate) was 54.8%, and the FE for C_3 product (acetone) was 5.7% at a current density of 65 mA^{-2} and a potential of -0.6 V vs RHE. In contrast, the FE for H_2, C_1, C_{2+} products on CuO NFs were shown in Fig. 4c. The FE for H_2 of CuO NFs is consistently higher than 30% in applied potentials from -0.3 V to -0.9 V, suggesting the strong competitive HER. Interestingly, the $FE_{hydrogen}$ of B-CuO NTs was substantially decreased and FE for C_{2+} (mainly ethanol and acetate) was enhanced accordingly, suggesting that the B dopant in B-CuO NTs could promote the selectivity of C_{2+} products. As shown in Fig. 4d, the $FE_{ethanol}$ of B-CuO NTs maintained above 40% in the potential range from -0.5 V to -0.7 V, and the maximum $FE_{ethanol}$ of 47% was achieved at -0.6 V vs RHE, which is highly selective for the formation of C_{2+} products. The CuO NFs only exhibits the maximum $FE_{ethanol}$ of 18.4% at -0.7 V vs RHE, indicating the low selectivity for C_{2+} production. As shown in Fig. 4e, the FE for the C_{2+}/C_1 products ratio of B-CuO NTs reaches 4.25 at -0.6 V, which is four times higher than that of CuO NFs at -0.7 V. The selectivity of CO_2RR to C_{2+} products on B-CuO NTs was over 45% in the potential range from -0.5 V to -0.7 V and it reach up to 60.5% at -0.6 V. The FE for C_{2+} of CuO NFs was below 28% in the potential from -0.3 V to -0.9 V. The partial current densities for C_{2+} products formation on B-CuO NTs and CuO NFs were shown in Fig. 4 f. The B-CuO NTs exhibits the greatly enhanced current density in the applied potential range, and show maximum current density for C_{2+} of 43 mA cm^{-2} at -0.6 V vs. RHE,

which is approximately 6 times higher than that obtained using CuO NFs (7 mAcm^{-2}). The results indicate that the B doping could significantly improve the conversion of CO_2 towards C_{2+} compounds. We further performed the electrochemical performance of B-CuO with different B contents. The B-CuO with different B contents were denoted as B-CuO-X (X = 0.25, 0.56 and 1.04 wt%). The morphologies of B-CuO-0.25 and B-CuO-1.04 were shown in Fig. S23. They both exhibit tubular nanofibers structures, which were similar with that of B-CuO-0.56 (Fig. 2). The corresponding CO_2RR performance of B-CuO-0.25, B-CuO-0.56 and B-CuO-1.04 samples were shown in Fig. S24. The B-CuO-0.56 shows the highest current density than those of B-CuO-0.25 and B-CuO-1.04 at the whole potential range. Meanwhile, the B-CuO-0.56 achieved the highest FE ($C_1 + C_2$) of 74.7% than those of B-CuO-0.25 (10.2%) and B-CuO-1.04 (43.1%). The influence of content of B on B-CuO demonstrate a volcano activity trend and the content of 0.56 wt% in B-CuO leads to the best electrocatalytic activity toward CO_2RR.

Electrochemically active surface area (ECSA) was evaluated by double layer capacitance (C_{dl}) using cyclic voltammetry (Fig. S25a). The C_{dl} value of B-CuO NTs was 4.2 mF cm^{-2}, which is larger than that of CuO NFs (3.3 mF cm^{-2}), suggesting that the B-CuO NTs possess more active sites due to the porous tubular structure. Electrochemical impedance spectroscopy (EIS) measurements (Fig. S25b) indicate that the Nyquist plots of B-CuO NTs has a smaller charge transfer resistance (R_{ct}) compared to CuO NFs, manifesting the fast electron transfer and
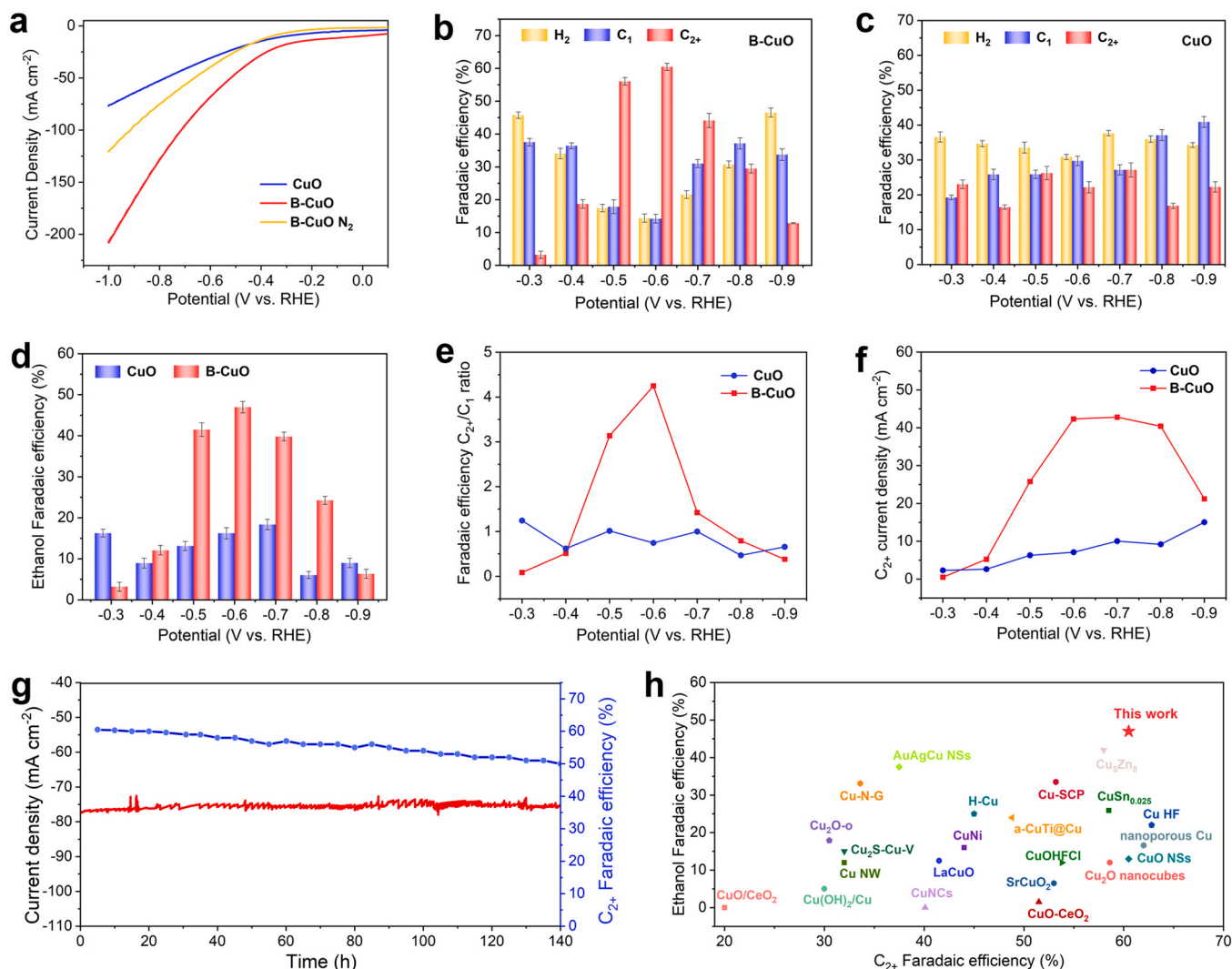
Fig. 4. (a) LSV curves of CuO NFs, B-CuO NTs in CO_2 and N_2 saturated 1 M KOH solution. FEs for H_2, C_1 and C_{2+} products on (b) B-CuO NTs and (c) CuO NFs. (d) $FE_{ethanol}$ and (e) FE for C_{2+}/C_1 products ratio of CuO NFs and B-CuO NTs. All the results were obtained by three independent tests with the standard deviation as error bars. (f) Partial current density of C_{2+} productions for CuO NFs and B-CuO NTs. (g) Long-term stability test of B-CuO NTs in 1 M KOH at − 0.6 V vs. RHE. (h) Comparison of FE for C_{2+} and $FE_{ethanol}$ of B-CuO NTs with other reported Cu-based catalysts.

kinetics for CO_2RR. Additionally, the long-term stability of B-CuO NTs was tested by chronoamperometry method at a constant applied voltage at − 0.6 V vs. RHE. Fig. 4 g shows that the B-CuO NTs display a steady current density around about 78 mA cm^{-2}, and the FEs for C_{2+} products were maintained above 52% for more than 120 h. In addition, the corresponding Cu 2p, B 1 s and O 1 s XPS spectra of B-CuO NTs after stability test still exhibit the characteristic peaks for B-CuO (Fig. S26a-c). XRD patterns of B-CuO NTs before and after long-term stability test show negligible changes (Fig. S26d). STEM-EDS mapping images of the B-CuO NTs after the long-term CO_2RR electrocatalysis test (Fig. S27) further confirm the tubular structures and elements distribution of B, Cu and O in B-CuO NTs. Besides, i-t curves at the potential range of − 0.3~− 0.9 V were presented in Fig. S28, and the highest current density (165 mA cm^{-2}) was obtained at the applied potential of − 0.9 V vs. RHE. Fig. 4 h displays the comparison of FE for C_{2+} and $FE_{ethanol}$ of B-CuO NTs in this work and recently reported superior Cu-based catalysts, suggesting that B-CuO NTs exhibits the excellent CO_2RR performance [28,41–57].

3.3. CO_2 reduction reaction mechanism

Figs. 5a and 5b reveal the in situ Raman spectra of CuO NFs and B-

CuO NTs performed at potentials from − 0.2 V to − 1.0 V to further explore the underlying mechanisms of the enhanced activity and selectivity toward C_{2+} products. At open-circuit potential (OCP), the characteristic Raman peaks for CuO phase emerged at 296 cm^{-1} and no other Raman peaks can be observed. The Raman peaks at 1070 cm^{-1} corresponds to the adsorbed carbonate (CO_3^{2-}) due to the CO_2 dissolved in KOH electrolyte [43]. This Raman peak can be observed on B-CuO NTs under − 0.2 V vs. RHE while it is emerged on CuO NFs under − 0.6 V vs. RHE, suggesting the fast kinetics of B-CuO NTs for CO_2RR. A new Raman peak emerged at 496 cm^{-1} suggest the Raman signal of *OCO⁻ intermediates appeared on CuO NFs, which is the key intermediate for producing formate in CO_2RR.[54] The results indicate that the CuO NFs tend to produce C_1 products, which is according with the electrocatalytic performances of CuO NFs (Fig. 4). Interestingly, two Raman peaks assigned to C≡O stretching of *CO appeared at 360 and 2080 cm^{-1} under − 0.2 V Vs. RHE [58,59], suggesting the key intermediates of *CO for C-C coupling and producing C_{2+} formed and adsorbed on B-CuO. Operando electrochemistry Raman measurements demonstrate the different generated intermediates on B-CuO NTs and CuO NFs, and further confirm the possible CO_2RR pathway of B-CuO NTs for C_{2+} production and CuO NFs for C_1 production.

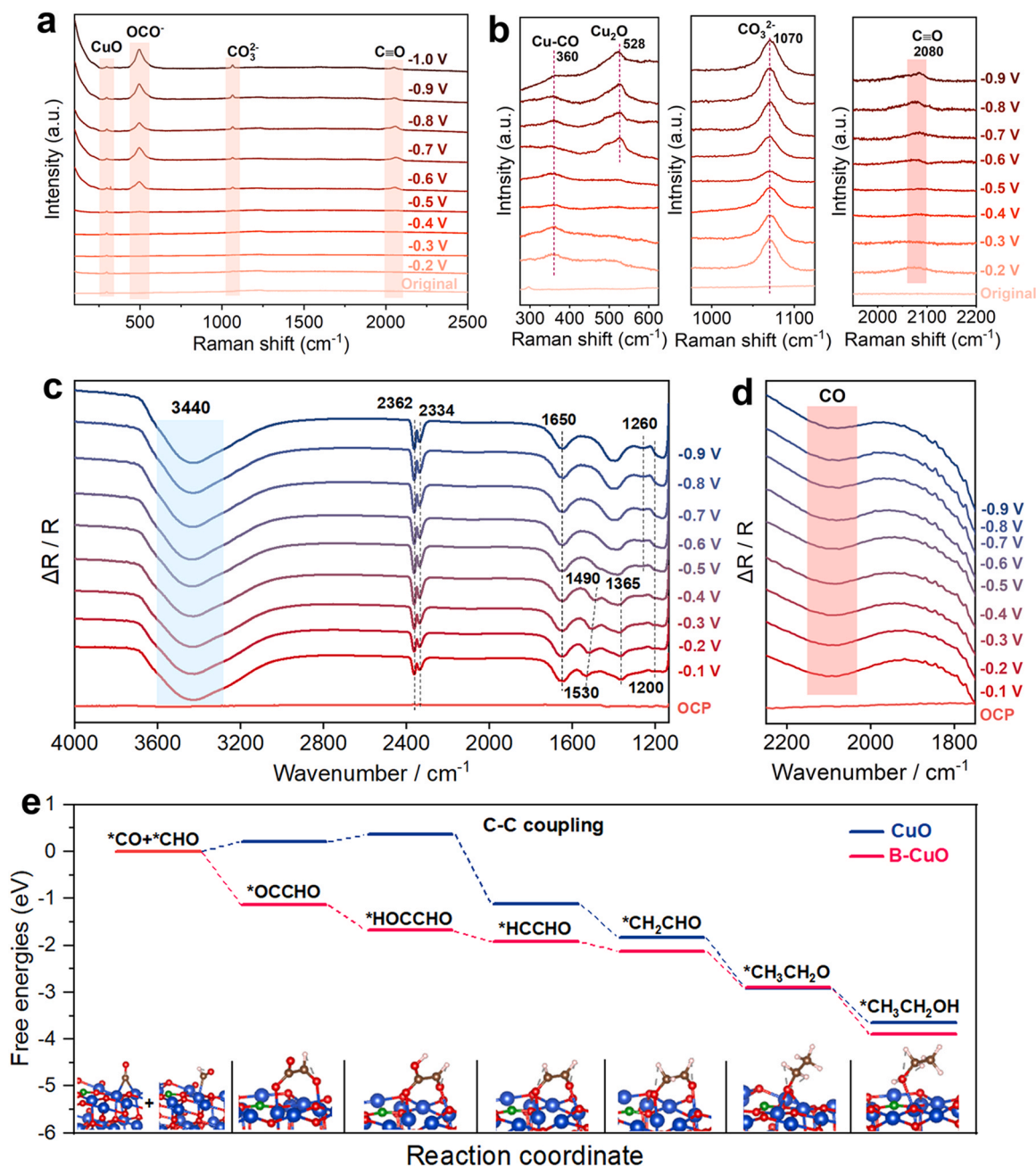*In situ* attenuated total reflectance infrared (ATR-IR) spectroscopy

Fig. 5. *In situ* Raman spectra of (a) CuO NFs and (b) B-CuO NTs electrode performed at various potentials during CO$_2$RR in 1 M KOH solution. (c) and (d) *In situ* ATR-IR spectra of B-CuO NTs performed at various potentials during CO$_2$RR in 1 M KOH solution. (e) Free energy diagrams of CO$_2$ to ethanol on B-CuO NTs. Inset display the optimal adsorption structure of intermediates on the surface of B-CuO NTs. The blue, red, green, brown and white balls represent Cu, O, B, C and H atoms.

were further employed to identify the reactive species of B-CuO NTs over the CO$_2$RR process. As shown in Fig. 5c, the peaks around 3440 and 1650 cm^{-1} represent the stretching vibration of O-H bonds and H-O-H bend of water. The peak at 2362 and 2334 cm^{-1} were ascribed to the OCO asymmetric stretching of CO$_2$ adsorbed on B-CuO NTs. The peaks emerged at 1530 and 1365 cm^{-1} under − 0.1 V vs. RHE can be assigned to the metal-carbonate species and the C-O stretch of *COOH, which are the important intermediates for formate formation [60,61]. With the increased potential from − 0.1 V to − 0.4 V, the peak at 1530 cm^{-1} exhibits positively shifts and gradually vanished at − 0.4 V Vs. RHE. Meanwhile, the peak at 1365 cm^{-1} also become weak with the increased potential to − 0.4 V, suggesting the reduced formation of *COOH intermediates on B-CuO NTs, and thus leading to the reduction in formate production. A broad band at 2080 cm^{-1} assigned to the *CO can be

obtained on B-CuO NTs, exhibiting strong capability for adsorbing the *CO intermediate (Fig. 5d). The strong ability for *CO adsorption facilitates the hydrogenation on B-CuO NTs to the *CHO intermediate (at 1250 cm^{-1}) and promotes the C-C coupling further to *OCCHO intermediate (1200 cm^{-1}) on B-CuO NTs via the proton-coupled electron transfer reactions [43,62]. *In situ* characterization results demonstrate that at potential below − 0.4 V vs. RHE, CO and formate were the main products on B-CuO NTs due to the 2-electron transfer dominated reduction. Multi-electron/proton transfer reduction gradually replace the 2-electron transfer process under low potentials (from −0.4 to −1.0 V), leading to the formation of C$_{2+}$ products. It is worth noting that the competitive HER was tempestuously proceeded under very low potential, and for example, the CuO NFs exhibit high FE$_{hydrogen}$ (more than 30%) in the potential range from − 0.4 V to − 0.9 V. However, the

B-CuO NTs displays the high FE for C_{2+} production even under very low potentials, suggesting the significantly suppressed HER process by B doping.

The Gibbs free energy (ΔG) for CO_2RR pathways on B-CuO NTs and the corresponding optimized configurations of adsorbed intermediates on CuO NFs and B-CuO NTs were shown in Fig. 5e. The Gibbs free energy of *CO coupling with *CHO on CuO NFs is decreased from 0.203 eV to -1.144 eV of B-CuO NTs, and meanwhile, B-CuO NTs shows the lower ΔG for further hydrogenation process than that of CuO NFs. These results clearly demonstrate that the polarized charge redistribution through B doping can suppress the *CHO transfer to C_1 products by reducing the energy barrier for OC-CHO coupling.

4. Conclusions

In summary, B-CuO NTs with low oxidation states have been successfully synthesized by using electrospinning technology and calcination. XPS and XAFS verified the strong electron transfers between B and Cu atoms in B-CuO NTs compared to the CuO NFs, leading to low oxidation state of Cu^{2+} towards Cu^+. The B-CuO NTs catalyst achieved an impressive FE for C_2 hydrocarbons above 60.5% including 47% of ethanol, which is superior higher than those of recently reported Cu-based catalysts. *In situ* Raman and ATR-FTIR spectra further demonstrate that the strong ability for *CO adsorption facilitates the hydrogenation to the *CHO intermediate and promotes the C-C coupling further to *OCCHO intermediate on B-CuO NTs via the proton-coupled electron transfer reactions. DFT calculations demonstrate that strong polarized charge redistribution by B doping could suppress the *CHO transfer to C_1 products by reducing the energy barrier for OC-CHO coupling.

CRediT authorship contribution statement

Han Zhu: Conceptualization, Supervision, Project administration, Funding acquisition, Writing – review & editing. **Jingwen Hu**: Investigation, Formal analysis, Data curation, Writing – original draft. **Zhili Zhang**: Investigation, Formal analysis, Data curation. **Zechao Zhuang**: Investigation, Formal analysis, Data curation. **Jiace Hao**: Investigation, Formal analysis, Data curation. **Fang Duan**: Formal analysis. **Shuanglong Lu**: Formal analysis. **Xiaofan Wang**: Formal analysis. **Mingliang Du**: Formal analysis.

Declaration of Competing Interest

The authors declare that they have no known competing financial interests or personal relationships that could have appeared to influence the work reported in this paper.

Data Availability

Data will be made available on request.

Acknowledgement

Appendix A. Supporting information

Supplementary data associated with this article can be found in the online version at doi:10.1016/j.apcatb.2023.123082.

References

[1] S. Navarro-Jaén, M. Virginie, J. Bonin, M. Robert, R. Wojcieszak, A.Y. Khodakov, Highlights and challenges in the selective reduction of carbon dioxide to methanol, Nat. Rev. Chem. 5 (2021) 564–579.

[2] J. Hao, Z. Zhuang, K. Cao, G. Gao, C. Wang, F. Lai, S. Lu, P. Ma, W. Dong, T. Liu, M. Du, H. Zhu, Unraveling the electronegativity-dominated intermediate adsorption on high-entropy alloy electrocatalysts, Nat. Commun. 13 (2022) 2662.

[3] B.A. Zhang, C. Costentin, D.G. Nocera, On the conversion efficiency of CO_2 electroreduction on gold, Joule 3 (2019) 1565–1568.

[4] X. Tan, C. Yu, Y. Ren, S. Cui, W. Li, J. Qiu, Recent advances in innovative strategies for the CO_2 electroreduction reaction, Energy Environ. Sci. 14 (2021) 765–780.

[5] B.H. Ko, F. Jiao, Well-defined model CO_2 electroreduction catalyst, Chem 6 (2020) 1506–1507.

[6] L. Zhang, J. Feng, S. Liu, X. Tan, L. Wu, S. Jia, L. Xu, X. Ma, X. Song, J. Ma, X. Sun, B. Han, Atomically dispersed Ni-Cu catalysts for pH-universal CO_2 electroreduction, Adv. Mater. 35 (2023), 2209590.

[7] R.G. Mariano, M. Kang, O.J. Wahab, I.J. McPherson, J.A. Rabinowitz, P.R. Unwin, M.W. Kanan, Microstructural origin of locally enhanced CO_2 electroreduction activity on gold, Nat. Mater. 20 (2021) 1000–1006.

8 N. Han, M. Sun, Y. Zhou, J. Xu, C. Cheng, R. Zhou, L. Zhang, J. Luo, B. Huang, Y. Li, Palladium-silver nanowires: alloyed palladium-silver nanowires enabling ultrastable carbon dioxide reduction to formate, Adv. Mater. 33 (2021), 2170027.

[9] S. Zhao, X. Lu, L. Wang, J. Gale, R. Amal, Carbon-based metal-free catalysts for electrocatalytic reduction of nitrogen for synthesis of ammonia at ambient conditions, Adv. Mater. 31 (2019), 1805367.

[10] D.C. Grills, M.Z. Ertem, M. McKinnon, K.T. Ngo, J. Rochford, Mechanistic aspects of CO_2 reduction catalysis with manganese-based molecular catalysts, Coord. Chem. Rev. 374 (2018) 173–217.

[11] Y. Wu, Z. Jiang, X. Lu, Y. Liang, H. Wang, Domino electroreduction of CO_2 to methanol on a molecular catalyst, Nature 575 (2019) 639–642.

[12] M.B. Ross, P. De Luna, Y. Li, C.-T. Dinh, D. Kim, P. Yang, E.H. Sargent, Designing materials for electrochemical carbon dioxide recycling, Nat. Catal. 2 (2019) 648–658.

[13] Z. Lyu, S. Zhu, M. Xie, Y. Zhang, Z. Chen, R. Chen, M. Tian, M. Chi, M. Shao, Y. Xia, Controlling the surface oxidation of Cu nanowires improves their catalytic selectivity and stability toward C_{2+} products in CO_2 reduction, Angew. Chem., Int. Ed. 60 (2021) 1909–1915.

[14] J. Hao, Z. Zhuang, J. Hao, K. Cao, Y. Hu, W. Wu, S. Lu, C. Wang, N. Zhang, D. Wang, M. Du, H. Zhu, Strain relaxation in metal alloy catalysts steers the product selectivity of electrocatalytic CO_2 reduction, ACS Nano 16 (2022) 3251–3263.

[15] J. Hao, H. Zhu, Z. Zhuang, Q. Zhao, R. Yu, J. Hao, Q. Kang, S. Lu, X. Wang, J. Wu, D. Wang, M. Du, Competitive trapping of single atoms onto a metal carbide surface, ACS Nano 17 (2023) 6955–6965.

[16] Z. Zhang, J. Hu, X. Zheng, W. Zhang, S. Lu, F. Duan, H. Zhu, M. Du, Solid-phase synthesis of ultra-small CuMo solid solution alloy for efficient electroreduction CO_2-to-C_{2+} productions, Chem. Commun. 59 (2023) 5221–5224.

[17] J. Hao, H. Zhu, Q. Zhao, J. Hao, S. Lu, X. Wang, F. Duan, M. Du, Interatomic electron transfer promotes electroreduction CO_2-to-CO efficiency over a CuZn diatomic site, Nano Res (2023), https://doi.org/10.1007/s12274-023-5577-2.

[18] Z. Gu, H. Shen, Z. Chen, Y. Yang, C. Yang, Y. Ji, Y. Wang, C. Zhu, J. Liu, J. Li, T.-K. Sham, X. Xu, G. Zheng, Efficient electrocatalytic CO_2 reduction to C_{2+} alcohols at defect-site-rich Cu surface, Joule 5 (2021) 429–440.

[19] Y. Sheng, Y. Guo, H. Yu, K. Deng, Z. Wang, X. Li, H. Wang, L. Wang, Y. Xu, Engineering under-coordinated active Sites with tailored chemical microenvironments over mosaic bismuth nanosheets for selective CO_2 electroreduction to formate, Small 19 (2023), 2207305.

[20] Y. Xu, Y. Guo, Y. Sheng, H. Yu, K. Deng, Z. Wang, X. Li, H. Wang, L. Wang, Selective CO_2 electroreduction to formate on polypyrrole-modified oxygen vacancy-rich Bi_2O_3 nanosheet precatalysts by local microenvironment modulation, Small (2023), 2300001.

[21] C. Xiao, J. Zhang, Architectural design for enhanced C_2 product selectivity in electrochemical CO_2 reduction using Cu-based catalysts: a review, ACS Nano 15 (2021) 7975–8000.

[22] W. Ma, X. He, W. Wang, S. Xie, Q. Zhang, Y. Wang, Electrocatalytic reduction of CO_2 and CO to multi-carbon compounds over Cu-based catalysts, Chem. Soc. Rev. 50 (2021) 12897–12914.

[23] B. Zhang, J. Zhang, M. Hua, Q. Wan, Z. Su, X. Tan, L. Liu, F. Zhang, G. Chen, D. Tan, X. Cheng, B. Han, L. Zheng, G. Mo, Highly electrocatalytic ethylene production from CO_2 on nanodefective Cu nanosheets, J. Am. Chem. Soc. 142 (2020) 13606–13613.

[24] L. Wan, X. Zhang, J. Cheng, R. Chen, L. Wu, J. Shi, J. Luo, Bimetallic Cu-Zn catalysts for electrochemical CO_2 reduction: phase-separated versus core-shell distribution, ACS Catal. 12 (2022) 2741–2748.

[25] X. Zhi, Y. Jiao, Y. Zheng, A. Vasileff, S.-Z. Qiao, Selectivity roadmap for electrochemical CO_2 reduction on copper-based alloy catalysts, Nano Energy 71 (2020), 104601.

[26] Q. Zhao, J.M.P. Martirez, E.A. Carter, Revisiting understanding of electrochemical CO_2 reduction on Cu(111): competing proton-coupled electron transfer reaction mechanisms revealed by embedded correlated wavefunction theory, J. Am. Chem. Soc. 143 (2021) 6152–6164.

[27] Y. Zhou, F. Che, M. Liu, C. Zou, Z. Liang, P. De Luna, H. Yuan, J. Li, Z. Wang, H. Xie, H. Li, P. Chen, E. Bladt, R. Quintero-Bermudez, T.-K. Sham, S. Bals, J. Hofkens, D. Sinton, G. Chen, E.H. Sargent, Dopant-induced electron localization drives CO_2 reduction to C_2 hydrocarbons, Nat. Chem. 10 (2018) 974–980.

[28] X.K. Lu, B. Lu, H. Li, K. Lim, L.C. Seitz, Stabilization of undercoordinated Cu sites in strontium copper oxides for enhanced formation of C_{2+} products in electrochemical CO_2 reduction, ACS Catal. 12 (2022) 6663–6671.

[29] X. Wang, Y. Jiang, K. Mao, W. Gong, D. Duan, J. Ma, Y. Zhong, J. Li, H. Liu, R. Long, Y. Xiong, Identifying an interfacial stabilizer for regeneration-free 300h rlectrochemical CO_2 teduction to C_2 products, J. Am. Chem. Soc. 144 (2022) 22759–22766.

[30] P.-P. Yang, X.-L. Zhang, F.-Y. Gao, Y.-R. Zheng, Z.-Z. Niu, X. Yu, R. Liu, Z.-Z. Wu, S. Qin, L.-P. Chi, Y. Duan, T. Ma, X.-S. Zheng, J.-F. Zhu, H.-J. Wang, M.-R. Gao, S.-H. Yu, Protecting copper oxidation state via intermediate confinement for selective CO_2 rlectroreduction to C_{2+} fuels, J. Am. Chem. Soc. 142 (2020) 6400–6408.

[31] G. Kresse, J. Furthmüller, Efficient iterative schemes for ab Initio total-energy calculations using a plane-wave basis set, Phys. Rev. B 54 (1996) 11169–11186.

[32] P.E. Blöchl, Projector augmented-wave method, Phys. Rev. B 50 (1994) 17953–17979.

[33] D. Joubert, From ultrasoft pseudopotentials to the projector augmented-wave method, Phys. Rev. B 59 (1999) 1758–1775.

[34] J.K. Nørskov, J. Rossmeisl, A. Logadottir, L. Lindqvist, J.R. Kitchin, T. Bligaard, H. Jónsson, Origin of the overpotential for oxygen reduction at a fuel-cell cathode, J. Phys. Chem. B 108 (2004) 17886–17892.

[35] L.C.P. Pérez, A. Arndt, S. Stojkovikj, I.Y. Ahmet, J.T. Arens, F. Dattila, R. Wendt, A. G. Buzanich, M. Radtke, V. Davies, K. Höflich, E. Köhnen, P. Tockhorn, R. Golnak, J. Xiao, G. Schuck, M. Wollgarten, N. López, M.T. Mayer, Determining structure-activity relationships in oxide derived Cu-Sn catalysts during CO_2 electroreduction using X-Ray spectroscopy, Adv. Energy Mater. 12 (2022), 2103328.

[36] Y. Ren, Y. Yang, L. Chen, L. Wang, Y. Shi, P. Yin, W. Wang, M. Shao, X. Zhang, M. Wei, Synergetic effect of Cu^0-Cu^+ derived from layered double hydroxides toward catalytic transfer hydrogenation reaction, Appl. Catal. B Environ. 314 (2022), 121515.

[37] K. Chu, Y.-P. Liu, Y.-H. Cheng, Q.-Q. Li, Synergistic boron-dopants and boron-induced oxygen vacancies in MnO_2 nanosheets to promote electrocatalytic nitrogen reduction, J. Mater. Chem. A 8 (2020) 5200–5208.

[38] Q. Wan, J. Zhang, B. Zhang, D. Tan, L. Yao, L. Zheng, F. Zhang, L. Liu, X. Cheng, B. Han, Boron-doped CuO nanobundles for electroreduction of carbon dioxide to ethylene, Green. Chem. 22 (2020) 2750–2754.

[39] K. Chu, F. Liu, J. Zhu, H. Fu, H. Zhu, Y. Zhu, Y. Zhang, F. Lai, T. Liu, A general strategy to boost electrocatalytic nitrogen reduction on perovskite oxides via the oxygen vacancies derived from A-site deficiency, Adv. Energy Mater. 11 (2021), 2003799.

[40] M. Fang, W. Ji, Y. Pi, P. Wang, Z. Hu, J.-F. Lee, H. Pang, Y. Li, Q. Shao, X. Huang, Aluminum-doped mesoporous copper oxide nanofibers enabling high-efficiency CO_2 electroreduction to multicarbon products, Chem. Mater. 34 (2022) 9023–9030.

[41] G. Iijima, T. Inomata, H. Yamaguchi, M. Ito, H. Masuda, Role of a hydroxide layer on Cu electrodes in electrochemical CO_2 reduction, ACS Catal. 9 (2019) 6305–6319.

[42] N.-T. Suen, Z.-R. Kong, C.-S. Hsu, H.-C. Chen, C.-W. Tung, Y.-R. Lu, C.-L. Dong, C.-C. Shen, J.-C. Chung, H.M. Chen, Morphology manipulation of copper nanocrystals and product selectivity in the electrocatalytic reduction of carbon dioxide, ACS Catal. 9 (2019) 5217–5222.

[43] X. Zhou, J. Shan, L. Chen, B.Y. Xia, T. Ling, J. Duan, Y. Jiao, Y. Zheng, S.-Z. Qiao, Stabilizing Cu_{2+} ions by solid solutions to promote CO_2 electroreduction to methane, J. Am. Chem. Soc. 144 (2022) 2079–2084.

[44] X. Su, Y. Sun, L. Jin, L. Zhang, Y. Yang, P. Kerns, B. Liu, S. Li, J. He, Hierarchically porous Cu/Zn bimetallic catalysts for highly selective CO_2 electroreduction to liquid C_2 products, Appl. Catal., B Environ. 269 (2020), 118800.

[45] N. Sakamoto, Y.F. Nishimura, T. Nonaka, M. Ohashi, N. Ishida, K. Kitazumi, Y. Kato, K. Sekizawa, T. Morikawa, T. Arai, Self-assembled cuprous coordination polymer as a catalyst for CO_2 electrochemical reduction into C_2 products, ACS Catal. 10 (2020) 10412–10419.

[46] B. Liu, X. Yao, Z. Zhang, C. Li, J. Zhang, P. Wang, J. Zhao, Y. Guo, J. Sun, C. Zhao, Synthesis of Cu_2O nanostructures with tunable crystal facets for electrochemical CO_2 reduction to alcohols, ACS Appl. Mater. Interfaces 13 (2021) 39165–39177.

[47] D. Zang, X.J. Gao, L. Li, Y. Wei, H. Wang, Confined interface engineering of self-supported Cu@N-doped graphene for electrocatalytic CO_2 reduction with enhanced selectivity towards eethanol, Nano Res 15 (2022) 8872–8879.

[48] Y. Zhu, Z. Gao, Z. Zhang, T. Lin, Q. Zhang, H. Liu, L. Gu, W. Hu, Selectivity regulation of CO_2 electroreduction on asymmetric AuAgCu tandem heterostructures, Nano Res 15 (2022) 7861–7867.

[49] X. Zhang, C. Liu, Y. Zhao, L. Li, Y. Chen, F. Raziq, L. Qiao, S.-X. Guo, C. Wang, G. G. Wallace, A.M. Bond, J. Zhang, Atomic nickel cluster decorated defect-rich copper for enhanced C_2 product selectivity in electrocatalytic CO_2 reduction, Appl. Catal., B Environ. 291 (2021), 120030.

[50] M. Li, N. Song, W. Luo, J. Chen, W. Jiang, J. Yang, Engineering surface oxophilicity of copper for electrochemical CO_2 reduction to ethanol, Adv. Sci. 10 (2023), 2204579.

[51] J.-J. Lv, M. Jouny, W. Luc, W. Zhu, J.-J. Zhu, F. Jiao, A highly porous copper electrocatalyst for carbon dioxide reduction, Adv. Mater. 30 (2018), 1803111.

[52] F. Hu, L. Yang, Y. Jiang, C. Duan, X. Wang, L. Zeng, X. Lv, D. Duan, Q. Liu, T. Kong, J. Jiang, R. Long, Y. Xiong, Ultrastable Cu catalyst for CO_2 electroreduction to multicarbon liquid fuels by tuning C-C coupling with CuTi subsurface, Angew. Chem., Inter, Ed. 60 (2021) 26122–26127.

[53] Y. Zhong, Y. Xu, J. Ma, C. Wang, S. Sheng, C. Cheng, M. Li, L. Han, L. Zhou, Z. Cai, Y. Kuang, Z. Liang, X. Sun, An artificial electrode/electrolyte interface for CO_2 electroreduction by cation surfactant self-assembly, Angew. Chem., Int, Ed. 59 (2020) 19095–19101.

[54] M. Li, Y. Ma, J. Chen, R. Lawrence, W. Luo, M. Sacchi, W. Jiang, J. Yang, Residual chlorine induced cationic active species on a porous copper electrocatalyst for highly stable electrochemical CO_2 reduction to C_{2+}, Angew. Chem., Int. Ed. 60 (2021) 11487–11493.

[55] X. Wang, K. Klingan, M. Klingenhof, T. Möller, J. Ferreira de Araújo, I. Martens, A. Bagger, S. Jiang, J. Rossmeisl, H. Dau, P. Strasser, Morphology and mechanism of highly selective Cu(II) oxide nanosheet catalysts for carbon dioxide electroreduction, Nat. Commun. 12 (2021) 794.

[56] J. Zhu, Y. Wang, A. Zhi, Z. Chen, L. Shi, Z. Zhang, Y. Zhang, Y. Zhu, X. Qiu, X. Tian, X. Bai, Y. Zhang, Y. Zhu, Cation-deficiency-dependent CO_2 electroreduction over copper-based ruddlesden-popper perovskite oxides, Angew. Chem., Int. Ed. 61 (2022), e202111670.

[57] C. Zhu, Y. Song, X. Dong, G. Li, A. Chen, W. Chen, G. Wu, S. Li, W. Wei, Y. Sun, Ampere-level CO_2 reduction to multicarbon products over a copper gas penetration electrode, Energy Environ. Sci. 15 (2022) 5391–5404.

[58] B. Zhang, Y. Chang, Y. Wu, Z. Fan, P. Zhai, C. Wang, J. Gao, L. Sun, J. Hou, Regulating *OCHO intermediate as rate-determining step of defective oxynitride nanosheets enabling robust CO_2 electroreduction, Adv. Energy Mater. 12 (2022), 2200321.

[59] Y. Song, J.R.C. Junqueira, N. Sikdar, D. Öhl, S. Dieckhöfer, T. Quast, S. Seisel, J. Masa, C. Andronescu, W. Schuhmann, B-Cu-Zn gas diffusion electrodes for CO_2 electroreduction to C_{2+} products at high current densities, Angew. Chem., Int. Ed. 60 (2021) 9135–9141.

[60] H. Cheng, S. Liu, J. Zhang, T. Zhou, N. Zhang, X.-S. Zheng, W. Chu, Z. Hu, C. Wu, Y. Xie, Surface nitrogen-injection engineering for high formation rate of CO_2 reduction to formate, Nano Lett. 20 (2020) 6097–6103.

[61] C. Liu, X.-D. Zhang, J.-M. Huang, M.-X. Guan, M. Xu, Z.-Y. Gu, In situ reconstruction of Cu-N coordinated MOFs to generate dispersive Cu/Cu_2O nanoclusters for selective electroreduction of CO_2 to C_2H_4, ACS Catal. 12 (2022) 15230–15240.

[62] E. Pérez-Gallent, M.C. Figueiredo, F. Calle-Vallejo, M.T.M. Koper, Spectroscopic observation of a hydrogenated CO dimer intermediate during CO reduction on Cu (100) electrodes, Angew. Chem., Int. Ed. 56 (2017) 3621–3624.